A Constitutive Model of Cyclic Viscoplasticity Considering Changes in Subsequent Viscoplastic Deformation due to the Evolution of Dislocation Structures

T. Mayama[a*] Research Associate
K. Sasaki[a] Associate Professor
H. Ishikawa[b] Professor

[a] Division of Human Mechanical Systems and Design, Hokkaido University, N13W8, Kita-ku, Sapporo, JAPAN

[b] Department of Mechanical Engineering, Kyusyu Sangyo University, Matsukadai 2-3-1, Higashi-ku, Fukuoka, JAPAN

Abstract

This paper presents a unified constitutive model for cyclic viscoplasticity and changes occurring in subsequent viscoplastic deformation due to the evolution of dislocation structures. The model considers the viscoplastic potential and a modified Ramberg-Osgood law. Stress is assumed to divide into three components: back stress (the center of the yield surface), flow stress (the radius of the yield surface), and viscous stress (overstress). The modification of the Ramberg-Osgood law is carried out employing memorized back stress. The applicability of the model to monotonic loading, pure creep, tension-compression cyclic loading, subsequent creep, and subsequent stress-relaxation were verified by comparing the predictions with experiments of Type 316L stainless steel at room temperature. The relationships between the internal variables in the model and the dislocation structures organized by cyclic deformations are also discussed.

Keywords: Constitutive model; Creep; Stress relaxation; Cyclic loading; Viscoplastic

material; Mechanical testing; Dislocation structures

*Tel.:+81-11-706-6416; fax:+81-11-706-6416.

E-mail address: mayama-t@eng.hokudai.ac.jp

1. Introduction

Micro-structures such as dislocation structures and crystallographic texture in materials strongly affect inelastic deformation which in turn affects the dislocation structures and crystallographic texture. A number of investigations of the relationship between macroscopic inelastic deformation and changes in dislocation structures have been reported (e.g. Yang and Lee 1993; Panin 1998; Bocher et al. 2001; Adams et al. 2004; Trivedi et al. 2004; Houtte et al. 2005; Zhang and Jiang 2005). However the relationship between dislocation-structures and macro-deformation is not sufficiently understood because there are complex hierarchical phenomena in the scale of dislocation structures which occur at an intermediate scale between discrete atomic scale and continuous macro scale.

Zhang and Jiang (2005) investigated reversibility of stress-strain responses and dislocation structures and found that the stress-strain curve is reversible when the magnitude of the loading is changed from high to low values or when the loading path is changed from nonproportional to proportional even when the dislocation substructures are not completely reversible. These results imply that a dislocation structure is not uniquely correlated to the stress-strain behavior during cyclic loading. Similarly, Mayama and Sasaki (2006) showed that dislocation structures are strikingly different during cyclic hardening and cyclic softening even when subjected to the similar stress-strain curves. Further, even when the stress-strain curves before the subsequent tests are very similar, the subsequent viscoplastic deformation such as creep and stress relaxation is different for different numbers of cycles of cyclic preloading. This leads to the conclusion that a model of cyclic viscoplasticity considering subsequent viscoplastic loading must account for both macroscopic deformation behavior and also for the dislocation structures.

Recently, experimental and theoretical investigations have led to the development of constitutive models considering the microstructure of materials (Estrin et al. 1996;

Estrin 1998; Estrin et al. 1998; Teodosiu and Hu 1995; Li et al. 2003; Uenishi and Teodosiu 2004; Bucher et al. 2004; Voyiadjis and Abed 2005; Bouvier et al. 2005; Abu Al-Rub et al. 2006; Brinckmann et al. 2006; Kuroda et al. 2006). Most of these recent physically-based models are developed based on concepts of dislocation structures rather than dislocation density as employed by classical Taylor hardening theory. Estrin (1998) proposed a dislocation density based constitutive model and extended it to describe deformation of all hardening regions. In that model dislocation densities are distinguished into a high dislocation density phase (cell wall) and a low dislocation density phase (cell interior), and so considers the dislocation structures. In the model proposed by Teodosiu and Hu (1995) dislocations are decomposed into currently active dislocations in the slip systems and dislocations in persistent dislocation structures connected with latent hardening. As a result, this model successfully describes large deformations with loading direction changes with only a small number of material parameters.

The present study proposes a constitutive model for cyclic viscoplasticity based on observations of dislocation structures. The model consists of a modified Ramberg-Osgood law and a kinematic hardening rule obtained from the viscoplastic potential. In the model, stress is assumed to divide into three parts: back stress (the center of the yield surface), time-independent flow stress, and time-dependent viscous stress (overstress) (e.g. Colak 2005; Colak and Krempl 2005). The internal variables in the model are defined considering the microstructures organized by inelastic deformation. The predictions by the proposed model are compared with the experimental results.

2. Formulation of Constitutive Model for Viscoplasticity

This section proposes a unified phenomenological model for viscoplasticity. The relationship between the model and microstructure will be discussed in section 4.

The viscoplastic potential is assumed as

$$F = \frac{H}{n+1}\left\langle \frac{\bar{\sigma} - R}{H} \right\rangle^{n+1}, \tag{1}$$

where $\langle\ \rangle$ indicates the MacAuley bracket $\langle x \rangle = \frac{1}{2}\left(x + |x|\right)$, H is the drag stress, R is the flow stress, and n is a material constant. The equivalent stress $\bar{\sigma}$ in Eq.(1) is represented as

$$\bar{\sigma} = \left\{ \tfrac{3}{2}\left(\boldsymbol{\sigma} - \mathbf{X}\right) : \mathbf{C} : \left(\boldsymbol{\sigma} - \mathbf{X}\right) \right\}^{1/2}. \tag{2}$$

where the colon ($:$) denotes the tensor product contracted twice, $\boldsymbol{\sigma}$ and $\mathbf{X}$ are the stress tensor and kinematic back stress tensor, respectively, and $\mathbf{C}$ is the plastic deformation induced anisotropic tensor of the 4th rank.

The normality hypothesis gives the following viscoplastic strain rate

$$\dot{\boldsymbol{\varepsilon}}^{v} = \frac{\partial F}{\partial \boldsymbol{\sigma}} = \left\langle \frac{\bar{\sigma} - R}{H} \right\rangle^{n} \frac{3}{2\bar{\sigma}} \mathbf{C} : \left(\boldsymbol{\sigma} - \mathbf{X}\right). \tag{3}$$

The viscoplastic work rate is defined as

$$\dot{W}^{v} = \bar{\sigma}\,\dot{\bar{\varepsilon}}^{v} = \left(\boldsymbol{\sigma} - \mathbf{X}\right) \cdot \dot{\boldsymbol{\varepsilon}}^{v}. \tag{4}$$

where the period ($\cdot$) denotes a scalar product.

Substituting Eq.(3) into (4) gives Eq.(5).

$$\dot{\bar{\varepsilon}}^{v} = \left\langle \frac{\bar{\sigma} - R}{H} \right\rangle^{n}. \tag{5}$$

Then, from Eqs.(3) and (5), the flow rule is given by Eq.(6).

$$\dot{\boldsymbol{\varepsilon}}^{v} = \frac{3\dot{\bar{\varepsilon}}^{v}}{2\bar{\sigma}} \mathbf{C} : (\boldsymbol{\sigma} - \mathbf{X}). \tag{6}$$

In Eqs.(1), (3), and (5), the flow stress R is assumed from conventional formulas, depending on the accumulated equivalent viscoplastic strain as

$$R = R_0 \left\{ 1 - \lambda \exp\left(- \frac{\int d\bar{\varepsilon}^{v}}{c} \right) \right\}, \tag{7}$$

where R_0, λ, and c are material constants. The accumulation of the viscoplastic strain leads to the increase of the number of mobile and immobile dislocations in inelastically deformed material. The strain hardening is considered as a consequence of the increase in dislocation density in classical dislocation theory. Therefore, the strain hardening and the accumulated viscoplastic strain are correlated in Eq.(7). The accumulation of the viscoplastic strain could be correlated to the increase of randomly scattering dislocations as discussed in section 4.

From Eq.(5) the equivalent stress becomes

$$\bar{\sigma} = H \left(\dot{\bar{\varepsilon}}^{v} \right)^{\frac{1}{n}} + R, \tag{8}$$

where H is assumed to be rate-dependent and n to be rate-independent. Eqs.(2) and (8) show that the equivalent stress may be considered the sum of 3 stress components;

the kinematic back stress X_{ij}, the viscous stress (or overstress) $H\left(\dot{\bar{\varepsilon}}^{v}\right)^{\frac{1}{n}}$, and the flow stress R. Therefore a differentiation of Eq.(8) with respect to time gives Eq.(9).

$$\dot{\bar{\sigma}} = \dot{H}\left(\dot{\bar{\varepsilon}}^{v}\right)^{\frac{1}{n}} + \frac{H\ddot{\bar{\varepsilon}}^{v}}{n}\left(\dot{\bar{\varepsilon}}^{v}\right)^{\frac{1-n}{n}} + \dot{R}. \tag{9}$$

Differentiation of Eq.(2) gives

$$\dot{\bar{\sigma}} = \frac{3}{2\bar{\sigma}}(\boldsymbol{\sigma}-\mathbf{X}):\mathbf{C}:\dot{\boldsymbol{\sigma}} + \frac{3}{4\bar{\sigma}}(\boldsymbol{\sigma}-\mathbf{X}):\dot{\mathbf{C}}:(\boldsymbol{\sigma}-\mathbf{X}) - \frac{3}{2\bar{\sigma}}(\boldsymbol{\sigma}-\mathbf{X}):\mathbf{C}:\dot{\mathbf{X}}. \tag{10}$$

The following Ziegler's law of evolution of the kinematic back stress is used here

$$\dot{\mathbf{X}} = (\boldsymbol{\sigma}-\mathbf{X})\dot{\mu}. \tag{11}$$

Substituting Eq.(11) into Eq.(10), Eq.(10) becomes

$$\dot{\bar{\sigma}} = \frac{3}{2\bar{\sigma}}(\boldsymbol{\sigma}-\mathbf{X}):\mathbf{C}:\dot{\boldsymbol{\sigma}} + \frac{3}{4\bar{\sigma}}(\boldsymbol{\sigma}-\mathbf{X}):\dot{\mathbf{C}}:(\boldsymbol{\sigma}-\mathbf{X}) - \frac{3}{2\bar{\sigma}}(\boldsymbol{\sigma}-\mathbf{X}):\mathbf{C}:(\boldsymbol{\sigma}-\mathbf{X})\dot{\mu}$$

$$= \frac{3}{2\bar{\sigma}}(\boldsymbol{\sigma}-\mathbf{X}):\mathbf{C}:\dot{\boldsymbol{\sigma}} + \frac{3}{4\bar{\sigma}}(\boldsymbol{\sigma}-\mathbf{X}):\dot{\mathbf{C}}:(\boldsymbol{\sigma}-\mathbf{X}) - \bar{\sigma}\dot{\mu}. \tag{12}$$

From Eqs.(9) and (12), $\dot{\mu}$ is expressed as

$$\dot{\mu} = \frac{3}{2\bar{\sigma}}(\boldsymbol{\sigma}-\mathbf{X}):\mathbf{C}:\dot{\boldsymbol{\sigma}} + \frac{3}{4\bar{\sigma}}(\boldsymbol{\sigma}-\mathbf{X}):\dot{\mathbf{C}}:(\boldsymbol{\sigma}-\mathbf{X})$$

$$-\frac{\dot{H}}{\bar{\sigma}}\left(\dot{\bar{\varepsilon}}^{v}\right)^{\frac{1}{n}}-\frac{H\ddot{\bar{\varepsilon}}^{v}}{n\bar{\sigma}}\left(\dot{\bar{\varepsilon}}^{v}\right)^{\frac{1-n}{n}}-\frac{\dot{R}}{\bar{\sigma}}. \qquad (13)$$

Substituting Eq.(13) into Eq.(11), the equation of evolution of back stress is

$$\dot{\mathbf{X}}=\left\{\frac{3}{2\bar{\sigma}}(\boldsymbol{\sigma}-\mathbf{X}):\mathbf{C}:\dot{\boldsymbol{\sigma}}+\frac{3}{4\bar{\sigma}}(\boldsymbol{\sigma}-\mathbf{X}):\dot{\mathbf{C}}:(\boldsymbol{\sigma}-\mathbf{X})\right.$$

$$\left.-\frac{\dot{H}}{\bar{\sigma}}\left(\dot{\bar{\varepsilon}}^{v}\right)^{\frac{1}{n}}-\frac{H\ddot{\bar{\varepsilon}}^{v}}{n\bar{\sigma}}\left(\dot{\bar{\varepsilon}}^{v}\right)^{\frac{1-n}{n}}-\frac{\dot{R}}{\bar{\sigma}}\right\}(\boldsymbol{\sigma}-\mathbf{X}). \qquad (14)$$

A constitutive model employing an Armstrong-Frederick type kinematic hardening rule, like the Chaboche model (1989), defines a plastic modulus, and models of this kind can describe non-linearity or roundness of the stress-strain relation. The present model, Eq.(14) is derived from the differentiation of the equivalent stress and the Ziegler law of evolution of back stress, and it is necessary to define a plastic modulus to express non-linearity of the stress-strain relation.

The following power law is used to represent the nonlinear plastic modulus.

$$\hat{\varepsilon}^{v}=\frac{K}{E}\left(\frac{\hat{\sigma}}{D}\right)^{m}\hat{\sigma}\ , \qquad (15)$$

where E is Young's modulus and K is a material constant, D and m are the reference stress and the exponent of hardening, and $\hat{\sigma}$ and $\hat{\varepsilon}^{v}$ are defined in Eqs.(16) and (17).

$$\hat{\sigma} = \left\{ \frac{3}{2} \left(\boldsymbol{\sigma}^{s'} - \mathbf{X}^{R'} \right) \cdot \left(\boldsymbol{\sigma}^{s'} - \mathbf{X}^{R'} \right) \right\}^{\frac{1}{2}} , \tag{16}$$

$$\hat{\varepsilon}^{v} = \sqrt{\left(\boldsymbol{\varepsilon}^{v} - \boldsymbol{\varepsilon}^{R} \right) \cdot \left(\boldsymbol{\varepsilon}^{v} - \boldsymbol{\varepsilon}^{R} \right)} , \tag{17}$$

here $\boldsymbol{\sigma}^{s'}$ and $\mathbf{X}^{R'}$ express the stress deviator component of $\boldsymbol{\sigma}^{s}$ and $\mathbf{X}^{R}$. The $\boldsymbol{\sigma}^{s}$, $\mathbf{X}^{R}$, and $\boldsymbol{\varepsilon}^{R}$ tensors are the quasi-static stress, the residual back stress, and the residual viscoplastic strain, respectively. Figure 1 is a schematic diagram of the concept of the constitutive model in the stress space. Now, $\mathbf{X}^{R}$ and $\boldsymbol{\varepsilon}^{R}$ are defined as the "memory point", the point where the loading direction changes, and $\mathbf{X}^{R}$ and $\boldsymbol{\varepsilon}^{R}$ are updated to the values of $\mathbf{X}$ and $\boldsymbol{\varepsilon}^{v}$. As a result, the memory point is the new origin of the stress of the power law as shown in Eq.(15). The new memory point $\mathbf{X}^{R}$ and $\boldsymbol{\varepsilon}^{R}$ maintains its value unless the loading direction is changed. Therefore, the differentiation of Eq.(15) becomes

$$\dot{\hat{\varepsilon}}^{v} = \frac{K}{E}(m+1)\left(\frac{\hat{\sigma}}{D} \right)^{m} \dot{\hat{\sigma}} . \tag{18}$$

As shown above, the proposed memory point concept is clear for uniaxial loading conditions. For multi-axial non-proportional loading conditions, however, various loading direction changes variously in contrast to proportional loading where only fully reversed direction change occurs. Therefore, further modification of the model and more detailed explanations are necessary when the proposed model is applied to non-proportional loading. For example, the authors have been developed the other form of the constitutive model for non-proportional loading experimental results in biaxial ratcheting loading, and proposed the non-proportionality parameters of loading path

(Mayama et al., 2004). In the present study, the non-proportionality parameters are not included in the model for simplicity because we conducted material tests only under uniaxial loading condition.

The plastic modulus G is defined as

$$G = \frac{\dot{\hat{\sigma}}}{\dot{\hat{\varepsilon}}^v} = 1 \Bigg/ \left\{ \frac{K}{E}(m+1)\left(\frac{\hat{\sigma}}{D}\right)^m \right\}. \tag{19}$$

In Eqs.(15), (18), and (19) D and m depend on the accumulated viscoplastic strain at the memory point, and are assumed as

$$D = D_i \left\{ 1 - \alpha_h \exp\left(-\frac{\int_i d\bar{\varepsilon}^v}{a_h} \right) + \alpha_s \exp\left(-\frac{\int_i d\bar{\varepsilon}^v}{a_s} \right) \right\}, \tag{20}$$

$$m = m_i \left\{ 1 - \beta \exp\left(-\frac{\int_i d\bar{\varepsilon}^v}{b} \right) \right\}, \tag{21}$$

where D_i, α_h, a_h, α_s, a_s, m_i, β, and b are material constants. The D_i and m_i values become D_0 and m_0 during the initial loading, and D_1 and m_1 after the first loading direction change. The changes in D_i and m_i are caused by deformation induced anisotropy, and it is not necessary to include an anisotropic coefficient in Eqs.(16) and (17).

The viscoplastic deformation induced anisotropy coefficient $\mathbf{C}$ in the subsequent yield surface formulation is represented in terms of viscoplastic strain as in Ishikawa (1997)

$$\mathbf{C} = \mathbf{I} + \mathbf{A}\,, \tag{22}$$

where $\mathbf{I}$ is the fourth-rank symmetric tensor, expressed by the Kronecker delta δ_{ij}:

$$I_{ijkl} = \frac{1}{2}\left(\delta_{ik}\delta_{jl} + \delta_{il}\delta_{jk} - \frac{2}{3}\delta_{ij}\delta_{kl} \right), \tag{23}$$

and

$$\mathbf{A} = \frac{\boldsymbol{\varepsilon}^{v} \otimes \boldsymbol{\varepsilon}^{v}}{\left| \boldsymbol{\varepsilon}^{v} \otimes \boldsymbol{\varepsilon}^{v} \right|} A_1 \left\{ \exp\left(A_2 \left| \boldsymbol{\varepsilon}^{v} \right| \left| \boldsymbol{\varepsilon}^{v} \right| \right) - 1 \right\}, \tag{24}$$

where A_1 and A_2 are material constants and $\otimes$ denotes the tensor product.

The following is a description of viscoplastic deformation using the present model. Figure 1 is a schematic diagram of the relationship between the stress $\boldsymbol{\sigma}$, the quasi-static stress $\boldsymbol{\sigma}^{s}$, the kinematic back stress $\mathbf{X}$, and the residual back stress $\mathbf{X}^{R}$. The relationship between the equivalent quasi-static stress rate $\dot{\bar{\sigma}}^{s}$ and the equivalent viscoplastic strain rate $\dot{\bar{\varepsilon}}^{v}$ from a "memory point" is determined by Eq.(18). Assuming that the directions of the stress rate $\dot{\boldsymbol{\sigma}}$ and quasi-static stress rate $\dot{\boldsymbol{\sigma}}^{s}$ are the same, the quasi-static stress $\boldsymbol{\sigma}^{s}$ is equal to the stress $\boldsymbol{\sigma}$ without the viscous stress (or overstress) $H\left(\dot{\bar{\varepsilon}}^{v}\right)^{\frac{1}{n}}$ $\left(= \left| \boldsymbol{\sigma} - \boldsymbol{\sigma}^{s} \right| \right)$, and the total stress is determined by adding the time-dependent viscous stress to the quasi-static stress in the direction of the quasi-static stress rate. Finally, the kinematic back stress is calculated by Eq.(14).

3. Experimental Results

3.1 Experimental procedure

Material tests to verify the applicability of the proposed model were conducted. The specimens used were a drawn tube of Type 316L stainless steel subjected to solution heat treatment. The tube had a 32mm outer diameter and a 6mm wall thickness and was

annealed by the manufacturer at 1070˚C for 5 minutes followed by water quenching. The chemical composition was 0.014C, 0.41Si, 1.14Mn, 0.028P, 12.15Ni, 16.22Cr, 2.06Mo, and Fe balance in weight percent. Tubular specimens were machined from this tube as shown in Fig.2. Young's modulus of the specimen at room temperature was E=200GPa.

A servo-controlled axial-torsional testing machine (Shimazu EHF-EB10), with a Shimazu 4825 controller and personal computer, were used for the computerized testing and data acquisition. Strain was measured using two strain gauges applied on opposite sides of the specimen. The axial force was measured using the load cell in the machine.

Four types of tests were conducted at room temperature: (1) monotonic loading tests at strain rates of 0.1, 0.01, or 0.001%/sec; (2) pure creep tests at stresses of 250, 275, or 300MPa for 1000sec; (3) a subsequent creep tests at a stress level of 330MPa after 10 or 50 cycles of tension-compression cyclic loading at the 0.01%/sec strain rate with a strain range of 1.0%; (4) a subsequent stress relaxation tests at 0.5% of the tensile strain after 10 or 50 cycles of tension-compression cyclic loading at the strain rate of 0.01%/sec with a strain range of 1.0%.

3.2 Monotonic loading tests

Figure 3 shows the stress-strain curves at room temperature of the monotonic loading tests under the 0.1%/sec (○), 0.01%/sec (□), and 0.001%/sec (×) strain rates, showing a strain rate dependence. The results show that Type 316L stainless steel is strain rate dependent at room temperature, i.e. monotonic loading under a faster strain rate lead to higher stress.

3.3 Pure Creep Test

Figure 4 shows pure creep curves at room temperature over 1000 seconds at stresses of 250MPa (○), 275MPa (□), and 300MPa (×) after the tensile loading at a stress rate of 5MPa/sec. Significant transient creep is observed at all stress levels.

3.4 Subsequent Creep Tests after Tension-Compression Cyclic Pre-loading

Figure 5 shows the stress-strain curve of cyclic loading with the strain range 1.0% under the strain rate 0.01%/sec. The stress-strain curve shows significant cyclic hardening. Figure 6 shows the relationship between the maximum peak stress and the number of cycles during the cyclic loading with the open circles (○) showing the experimental results. The maximum peak stress initially increases and then decreases after the 20^{th} cycle. As shown in Fig.6, the maximum peak stresses of the 10 and 50 cycles are almost the same values. Figure 7 shows the stress-strain curves of the 10 and 50 cycles. The stress-strain curves are also almost the same. This suggests that there is no difference between the macroscopic experimental behaviors of the 10 and 50 cycles. It should be noted that the cyclic hardening of austenitic stainless steel depends on the strain range as shown by Kang et al. (2003). The strain hardening with larger strain ranges is more significant than that with smaller strain ranges, which means that the transition from cyclic hardening to cyclic softening is also strain range dependent. Therefore, the number of cycles and cyclic hardening and softening behavior shown in Figs. 6 and 7 are valid only for the present experimental condition. In the present study, we have not concentrate on the amplitude-dependent cyclic loading behavior. In order to understand the essential mechanism in cyclic plasticity, however, the further investigations have to be made on the relationship between the strain amplitude-dependent cyclic loading and the organization of dislocation structures.

Figure 8 shows the subsequent creep curves after the 10 cycles (○) and 50 cycles (□) of cyclic loading shown in Figs.6 and 7. The creep curves are different although the stress-strain curves after 10 and 50 cycles are the same as shown in Fig.7.

3.5 Subsequent Stress Relaxation Tests after Tension-Compression Cyclic Pre-loading

Figure 9 shows the relationships between relaxed stress and time during the subsequent stress relaxation tests at a strain 0.5% after 10 cycles (○) and 50 cycles (□) of cyclic loading as shown in Figs.6 and 7. The relationships are clearly different

although the stress just before the each relaxation tests is the same (310MPa). Therefore, the amounts of the relaxed stress decreases with the increase in the number of cycle of the cyclic preloading while the stress-strain curves after 10 cycles and 50 cycles are the same as shown in Fig.7.

4. Numerical Descriptions and Discussion

The subsequent creep and stress relaxation in Figs.8 and 9 show that the subsequent viscoplastic deformation on Type 316L stainless steel depends on the cyclic preloading. These results are similar to the results for Type 304 stainless steel in a previous paper (Mayama and Sasaki 2006). Both Type 304 and Type 304 stainless steels show qualitatively similar cyclic hardening and softening, the subsequent creep, the subsequent stress relaxation, and dislocation structural changes. From the experimental results for Type 304 stainless steel, it has been assumed that the different subsequent deformations are caused by different dislocation structures forming due to cyclic preloading. The dislocation structures initially increase randomly and cyclic hardening occurs. After some number of cycles, the randomly configured dislocations organize into cell structures, which are low energy dislocation structures caused by the cyclic loadings and the result is a cyclic softening.

The present study also observed dislocation structures after the cyclic loading of Type 316L stainless steel. Figs.10 (a) and (b) show the dislocation structures after 10 and 50 cycles of tension-compression cyclic loading. The dislocation structure after 10 cycles shows scattered dislocations and after 50 cycles there are dislocation cell structures similar to those in the previous paper (Mayama and Sasaki 2006). The subsequent creep and stress relaxation cannot be predicted from conventional phenomenological models because these macroscopic models assume that the amount of viscoplastic deformation depends on only the strain (or stress) rate. To predict subsequent creep and stress relaxation, a model must consider the loading history as it

relates to the microstructure.

The experimental results and the observed dislocation structure show that the peak stress during the cyclic loading and the amount of viscous deformation decrease and the dislocations organize cell structure after the sufficiently large number of cycles of the cyclic loading. The decreases of the peak stress and the viscous deformation suggest that the viscous stress $H\left(\dot{\varepsilon}^{v}\right)^{1/n}$ (or over stress) should decrease in Eq. (8). The observation suggests that the dislocation cell structure contribute to the cyclic softening while the uniformly scattering dislocations are seen during cyclic hardening. The accumulation of the viscoplastic strain may correlated to the cell structure organization because the cell structure has been organized after the large number of cyclic hardening. In this study, therefore, the decrease of the viscous stress (or over stress) is modeled as the scalar function of the accumulated viscoplastic strain H in Eqs.(8) and (9) as:

$$H = H_{sat}\left\{1+\eta\exp\left(-\int d\bar{\varepsilon}^{v}/h_{s}\right)\right\} \qquad (25),$$

where H_{sat}, η, and h_s are material parameters.

The experiments in this study are for the uniaxial condition with small strains. For uniaxial isotropic loading, Eqs. (14) and (18) reduce to

$$\dot{X}_{tc} = \dot{\sigma}_{tc} - \dot{H}\left(\left|\dot{\varepsilon}_{tc}^{v}\right|\right)^{\frac{1}{n}} - \frac{H\left|\dot{\bar{\varepsilon}}_{tc}^{v}\right|}{n}\left(\left|\dot{\varepsilon}_{tc}^{v}\right|\right)^{\frac{1-n}{n}} - \dot{R}, \qquad (26)$$

$$\dot{\varepsilon}_{tc}^{v} = \frac{\dot{\sigma}_{tc}}{G} = \frac{K}{E}(m+1)\left(\frac{\left|\sigma_{tc}^{s} - X_{tc}^{R}\right|}{D}\right)^{m}\dot{\sigma}_{tc}, \qquad (27)$$

where ε_{tc}, σ_{tc}, and X_{tc} are the tension-compression axial components of the strain, stress, and back stress, respectively.

Using Eqs.(26), (27), and the internal fuctions Eqs.(7), (20), (21), and (25) with the material parameters as shown in Table 1, numerical calculations were conducted.

In Fig.3 the solid lines show the calculated stress-strain curves and the broken line is the calculated back stress arising from the monotonic loading tests. The predicted stress-strain curves agree well with the experimental results. The back stress does not change due to the strain rate as would be expected when the static hardening surface is not affected by strain rate.

In Fig.4 the solid lines show the calculated creep curves, and the experimental results and predictions show good agreement.

In Fig.6 the solid line shows the model calculations of the relationship between the maximum peak stress and the number of cycles during cyclic loading. The model predictions and the experimental results show good agreement. In Fig.11 the open circles (○) and the solid line show the predicted stress-strain curves after the 10 and 50 cycles. The predictions for the stress-strain curves agree well with each other, similar to the experimental results in Fig.7.

In Fig.8, the solid lines show the predictions of the subsequent creep curves after cyclic preloading. In Fig.9 the solid lines show the predictions of the subsequent stress relaxation curves after cyclic preloading. Figures 8 and 9 show the good applicability of the proposed model to the different subsequent viscoplastic deformations following cyclic preloading.

Figure 12 is a schematic diagram of the changes in yield and viscous surfaces with 10 and 50 cycles of preloading. The very similar stress-strain curves after 10 and 50 cycles in Fig.7 suggest that the back stress-strain trajectories should also be similar, and the similar peak stresses at the 10 and 50 cycles suggest that specimens may display similar total values of flow stress R and viscous stress $H\left(\dot{\varepsilon}^{v}\right)^{1/n}$ (or over stress). The total value of the flow stress R and viscous stress $H\left(\dot{\varepsilon}^{v}\right)^{1/n}$ equals the effective stress $\left|\boldsymbol{\sigma}-\mathbf{X}\right|$. Therefore, ignoring anisotropy in Eq.(8) the following equation is

obtained

$$\left|\boldsymbol{\sigma}-\mathbf{X}\right|_{10^{th}} = R_{10^{th}} + H_{10^{th}}\left(\dot{\bar{\varepsilon}}^{v}\right)^{1/n} = R_{50^{th}} + H_{50^{th}}\left(\dot{\bar{\varepsilon}}^{v}\right)^{1/n} = \left|\boldsymbol{\sigma}-\mathbf{X}\right|_{50^{th}}, \qquad (28)$$

where $R_{10^{th}}$, $R_{50^{th}}$, $H_{10^{th}}\left(\dot{\bar{\varepsilon}}^{v}\right)^{1/n}$, $H_{50^{th}}\left(\dot{\bar{\varepsilon}}^{v}\right)^{1/n}$, $\left|\boldsymbol{\sigma}-\mathbf{X}\right|_{10^{th}}$, and $\left|\boldsymbol{\sigma}-\mathbf{X}\right|_{50^{th}}$ are the flow stresses, viscous stresses, and effective stresses at the 10th and 50th cycle of preloading, respectively.

The experimental results of the different subsequent deformations shown in Figs. 8 and 9 suggest that the viscous stress at the 10th cycle should be larger than that at the 50th cycle. Therefore, considering Eq.(28), the following relations are obtained,

$$H_{10^{th}} > H_{50^{th}} \quad , \quad R_L < R_H . \qquad (29)$$

These changes in internal variables may be correlated to the changes in microstructures. From the TEM observations of dislocation structures in Fig.10 and the previous paper (Mayama and Sasaki 2006), it can be assumed that the flow stress is related to the density of a randomly increased number of scattered dislocations, which leads to the cyclic hardening and larger time-dependent deformations, and the viscous stress is related to the organization of dislocation structures, which leads to the cyclic softening and the decrease in time dependent deformation. The cyclic hardening and larger time-dependent deformation would appear to be contradictory phenomena. However, they can be explained by some dislocation structures posing limited obstacles for cyclic loading and these dislocation structures not acting as obstacles to subsequent time-dependent deformation. In other words, hardening and softening could depend on the loading conditions. A similar conclusion has been suggested elsewhere (El-Danaf et al. 2001, Mayama and Sasaki 2006).

Thielen et al. (1976) have conducted the strain controlled low cycle fatigue of a 4140 steel at room temperature. They discuss that transmission electron microscopy shows cyclic softening resulted in part from rearrangement of the dislocation structure and reduction of dislocation density. Recent investigations also suggest that the organization of dislocation structures could lead to cyclic softening (Fujii et al. 2001, Petrenec et al. 2006). Fujii et al. (2001) have studied the cyclic softening after the initial hardening of a polycrystalline 3003 aluminum alloy. In their high stress amplitude cyclic loading tests, cell structures are dominant at the final stage. Petrenec et al. (2006) have observed the dislocation structure in polycrystalline X10CrAl24 ferritic stainless steel cyclically strained with constant plastic strain amplitude. In their high-amplitude cyclic loading, wall, labyrinth and cell structures are produced. They conclude that increase in the volume fraction occupied by wall structures is responsible for the cyclic softening. Therefore, it might be reasonable to correlate the formation of the cell structures to the cyclic softening in the present study.

5. Conclusions

This study proposes a unified constitutive model for cyclic plasticity and subsequent viscoplastic deformation. The model employs the viscoplastic potential and static hardening surface. To describe the subsequent deformation after cyclic preloading, internal variables relating to micro-scale dislocation structures were introduced. To verify the proposed model experiments of monotonic loading, pure creep, cyclic loading, and subsequent viscoplastic deformation of Type 316L stainless steel at room temperature were predicted by the model, and the following conclusions were obtained:

(1) A constitutive model for cyclic viscoplasticity was constructed assuming that the cyclic hardening is related to a macroscopic isotropic hardening and an increase in microscopic dislocation density, and the cyclic softening is related to a decrease in macroscopic viscous stress (or overstress) and the organization of microscopic low

energy dislocation structures (cell structures).

(2) The proposed model describes the monotonic loading under constant strain rates, pure creep at three different stress levels, and cyclic loading in a constant strain range under a constant strain rate. The relationship between the peak stresses and the number of cycles during the cyclic loading is well predicted as is the stress-strain curve of the cyclic loading.

(3) Assuming that both the flow stress and viscous stress (or overstress) could change in value during cyclic loading, internal functions of accumulated viscoplastic strain were incorporated. Consequently, the subsequent viscoplastic deformation is well predicted by the model.

(4) The constitutive modeling and the observations of dislocation structures suggest that the increase of flow stress and the decrease of viscous stress could be correlated to the increase in randomly scattered dislocations and an organization of dislocation structures.

References

Abu Al-Rub, R. K., Voyiadjis, G. Z., A physically based gradient plasticity theory. Int. J. Plasticity 22, 654-684.

Bocher, L., Delobelle, P., Robinet, P., Feaugas, X., 2001. Mechanical and microstructural investigations of an austenitic stainless steel under non-proportional loadings in tension-torsion-internal and external pressure. Int. J. Plasticity 17, 1491-1530.

Bouvier, S., Alves, J. L., Oliveira, M. C., Menezes, L. F., 2005. Modelling of anisotropic work-hardening behaviour of metallic materials subjected to strain-path changes. Comp. Mater. Sci. 32, 301-315.

Brinckmann, S., Siegmund, T., Huang, Y., A dislocation density based strain gradient model. Int. J. Plasticity 22, 1784-1797.

Bucher, A., Görke, U. –J., Kreiβig, R., 2004. A material model for finite elasto-plastic deformations considering a substructure. Int. J. Plasticity 20, 619-642.

Chaboche, J. L., 1989. Constitutive equations for cyclic plasticity and cyclic viscoplasticity. Int. J. Plasticity 5, 247-302.

Colak, O. U., 2005. Modeling deformation behavior of polymers with viscoplasticity theory based on overstress. Int. J. Plasticity 21, 145-160.

Colak, O. U., Krempl, E., 2005. Modeling of the monotonic and cyclic Swift effects using an isotropic, finite viscoplasticity theory based on overstress (FVBO). Int. J. Plasticity 21, 573-588.

El-Danaf, E., Kalidindi, S.R., Doherty, R.D., 2001. Influence of deformation path on the strain hardening behavior and microstructure evolution in low SFE FCC metals. Int. J. Plasticity 17, 1245-1265.

Estrin, Y., Braasch, H., and Brechet, Y., 1996. A dislocation density based constitutive model for cyclic deformation. J. Eng. Mater. Technol. 118, pp.441-447.

Estrin, Y., 1998. Dislocation theory based constitutive modelling: foundations and

applications. J. Mater. Proc. Technol. 80-81, pp.33-39.

Estrin, Y., Tóth, L. S., Molinari, A., Bréchet, Y., 1998. A dislocation-based model for all hardening stages in large strain deformation. Acta Mater. 46, pp.5509-5522.

Fujii, T., Watanabe, C., Nomura, Y., Tanaka, N., Kato, M., 2001, Microstructural evolution during low cycle fatigue of a 3003 aluminum alloy. Mater. Sci. Eng. A319-321, 592-596.

Ho, K. C., Lin, J., Dean, T. A., 2004. Modelling of springback in creep forming thick aluminum sheets. Int. J. Plasticity 20, 733-751.

Houtte, P. V., Li, S., Seefeldt, M., Delannay, L., 2005. Deformation texture prediction: from the Taylor model to the advanced Lamel model. Int. J. Plasticity 21, 589-624.

Ishikawa, H., 1997. Subsequent yield surface probed from its current center. Int. J. Plasticity 13, 533-549.

Kang, G., Ohno, N., Nebu, A., 2003. Constitutive modeling of strain range dependent cyclic hardening. Int. J. Plasticity 19, 1801-1819.

Kuroda, M., Uenishi, A., Yoshida, H., Igarashi, A., 2006. Ductility of interstitial-free steel under high strain rate tension: Experiments and macroscopic modeling with a physically-based consideration. Int. J. Solids Structures 43, 4465-4483.

Li, S., Hoferlin, E., Bael, A. V., Houtte, P. V., Teodosiu, C., 2004. Finite element modeling of plastic anisotropy induced by texture and strain-path change. Int. J. Plasticity 20, pp.915-936.

Lin, R.C., Brocks, W., 2004. On a finite strain viscoplastic theory based on a new internal dissipation inequality. Int. J. Plasticity 20, 1281-1311.

Mayama, T., Sasaki, K., Ishikawa, H., 2004. Biaxial ratchetting deformation of type 304 stainless steel: effect of memorization of back stress. J. Mech. Eng. Sci. 218C, 901-908.

Mayama, T., Sasaki, K., 2006. Investigation of subsequent viscoplastic deformation of austenitic stainless steel subjected to cyclic preloading. Int. J. Plasticity 22, 374-390.

Panin, V. E. (Ed.), 1998. Physical mesomechanics of heterogeneous media and

computer-aided design of materials, Cambridge International Science Publishing, UK.

Petrenec, M., Polák, J., Obrtlík, K., Man, J., 2006. Dislocation structures in cyclically strained X10CrAl24 ferritic steel, Acta Mater. 54, 3429-3443.

Taylor, G. I., 1934. The mechanism of plastic deformation of crystals. Part I. – theoretical. Proc. R. Soc., London A 145, 362-387.

Teodociu, C., Hu, Z., 1995. Evolution of the intragranular microstructure at moderate and large strains : Modelling and computational significance. Proc. NUMIFORM '95, 173-182.

Thielen, P. N., Fine, M. E., Fournelle, R. A., 1976. Cyclic stress strain relations and strain-controlled fatigue of 4140 steel. Acta Metall. 24, 1-10.

Trivedi, P., Field, D. P., Weiland, H., 2004. Alloying effects on dislocation substructure evolution of aluminum alloys. Int. J. Plasticity 20, 459-476.

Uenishi, A., Teodosiu, C., 2004. Constitutive modeling of the high strain rate behaviour of interstitial-free steel. Int. J. Plasticity 20, 915-936.

Voyiadjis, G. Z., Abed, F. H., 2005. Microstructural based models for bcc and fcc metals with temperature and strain rate dependency. Mech. Mater. 37, 355-378.

Yang, W., Lee, W. B., 1993. MRE Mesoplasticity and its applications, Springer-Verlag, Berlin.

Zhang, J., Jiang, Y., 2005. An experimental investigation on cyclic plastic deformation and substructures of polycrystalline copper. Int. J. Plasticity 21, 2191-2211.

Captions of figures and tables

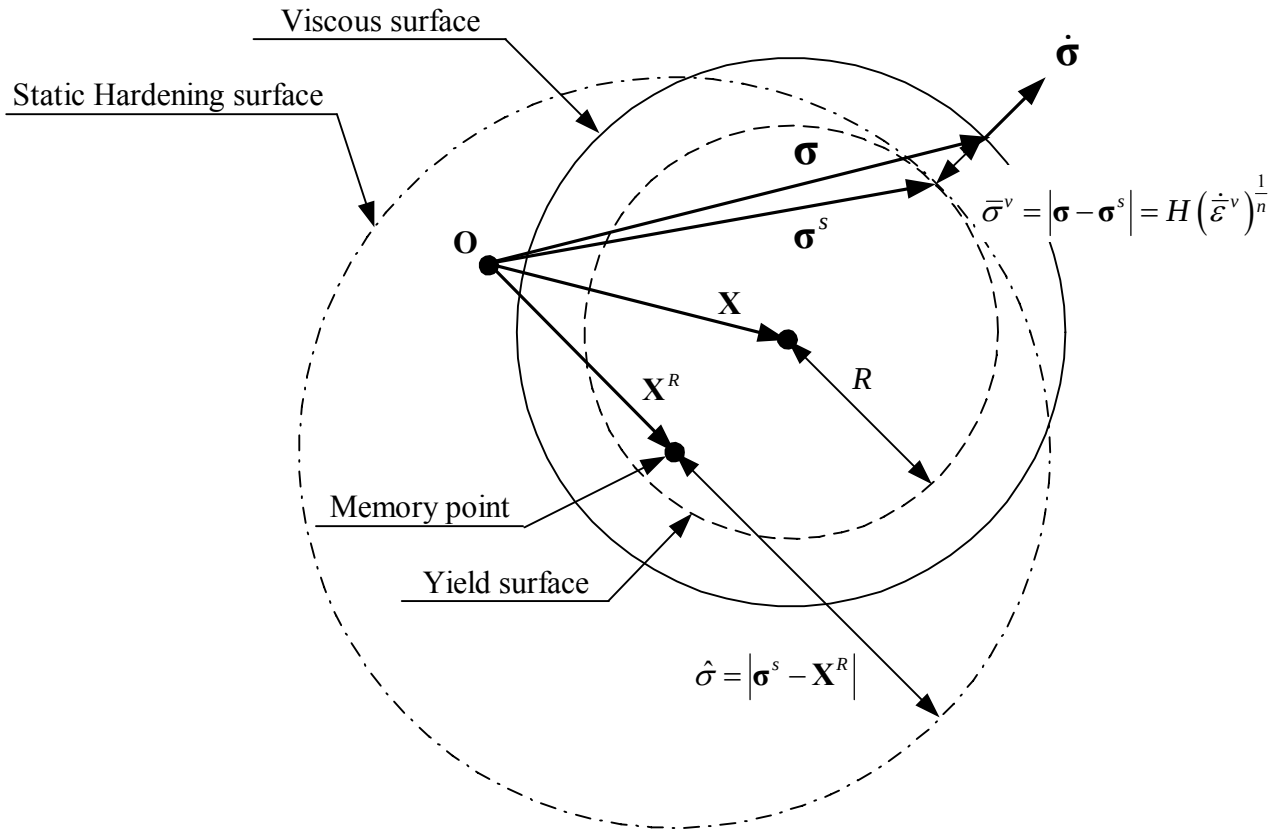

Fig.1 Schematic diagram of the constitutive model in the stress space

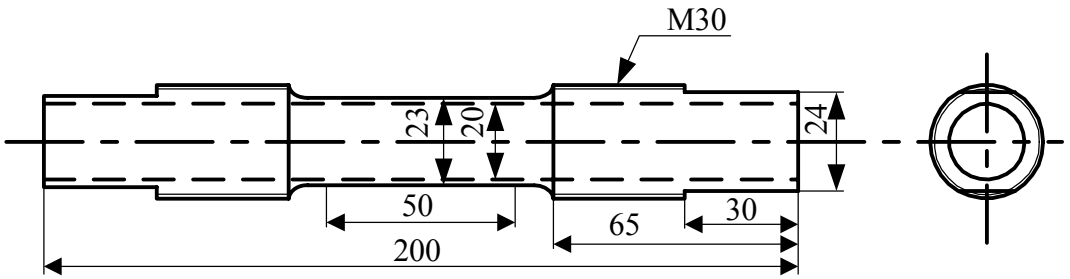

Fig.2 The geometry of specimens

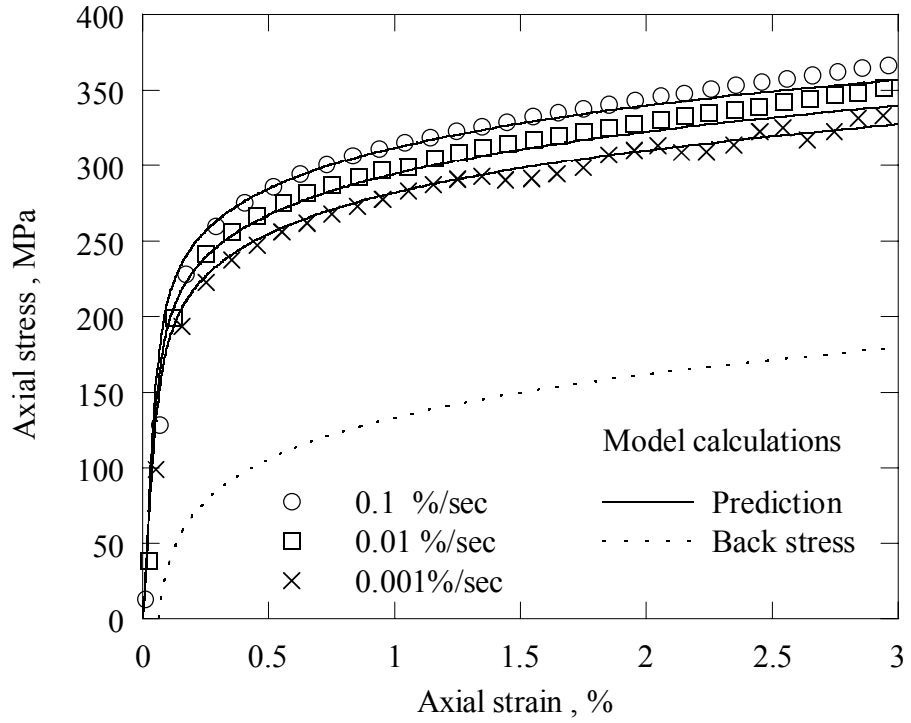

Fig.3 Stress-strain curves of monotonic loading tests under strain rates of 0.1, 0.01, and 0.001%/sec with model predictions

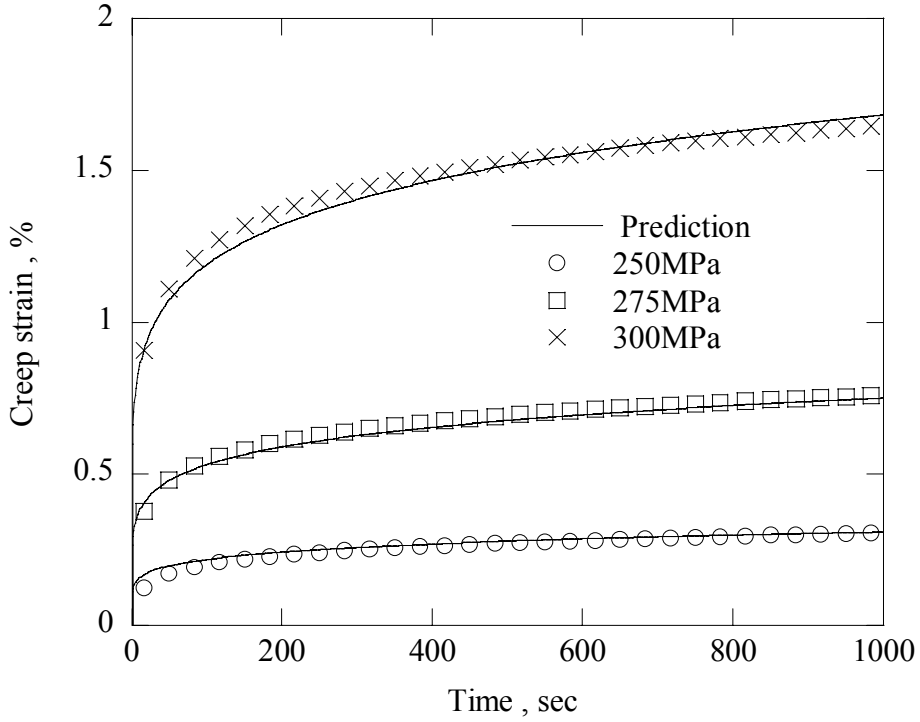

Fig.4 Creep curves of pure creep tests at stresses of 250, 275, and 300MPa with model predictions

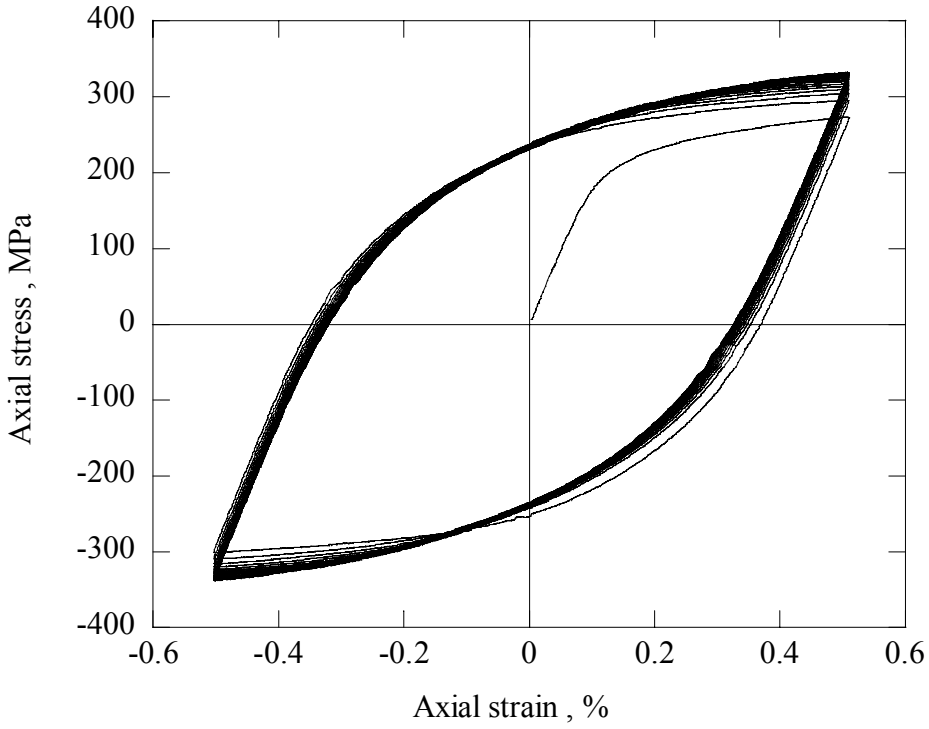

Fig.5 Stress-strain curve of cyclic loading under a strain rate of 0.01%/sec with strain amplitude 0.5%

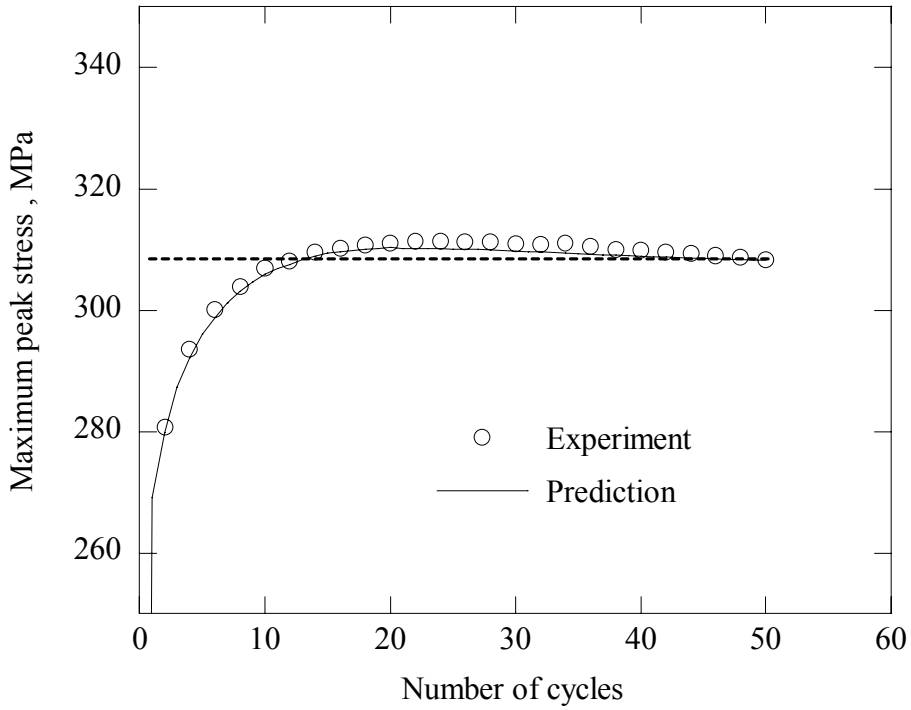

Fig.6 Maximum peak stresses versus the number of cycles during cyclic loading under a strain rate of 0.01%/sec with strain amplitude 0.5% with model predictions

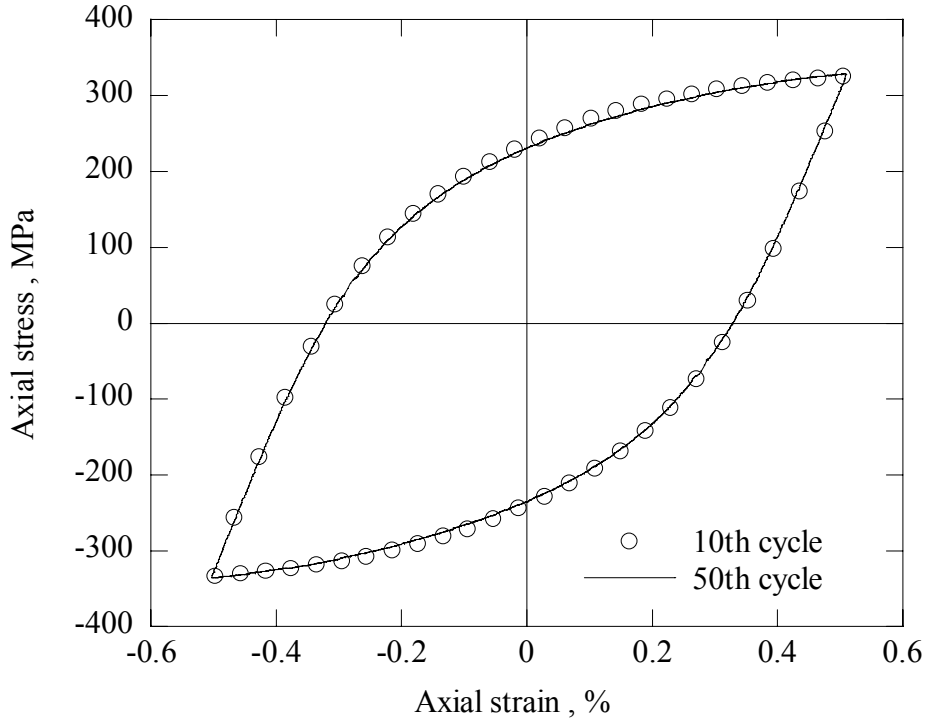

Fig.7 The measured stress-strain curves at the 10^{th} and 50^{th} cycle of cyclic loading under a strain rate of 0.01%/sec with strain amplitude 0.5%

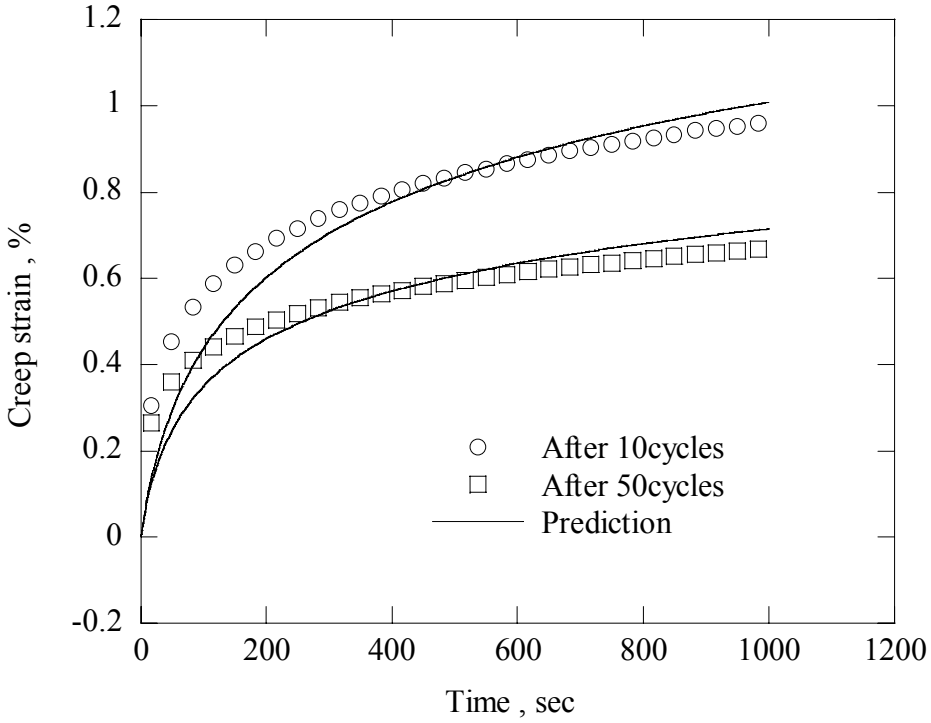

Fig.8 Creep curves of subsequent creep tests at a stress of 330MPa after 10 and 50 cycles of cyclic loading with model predictions

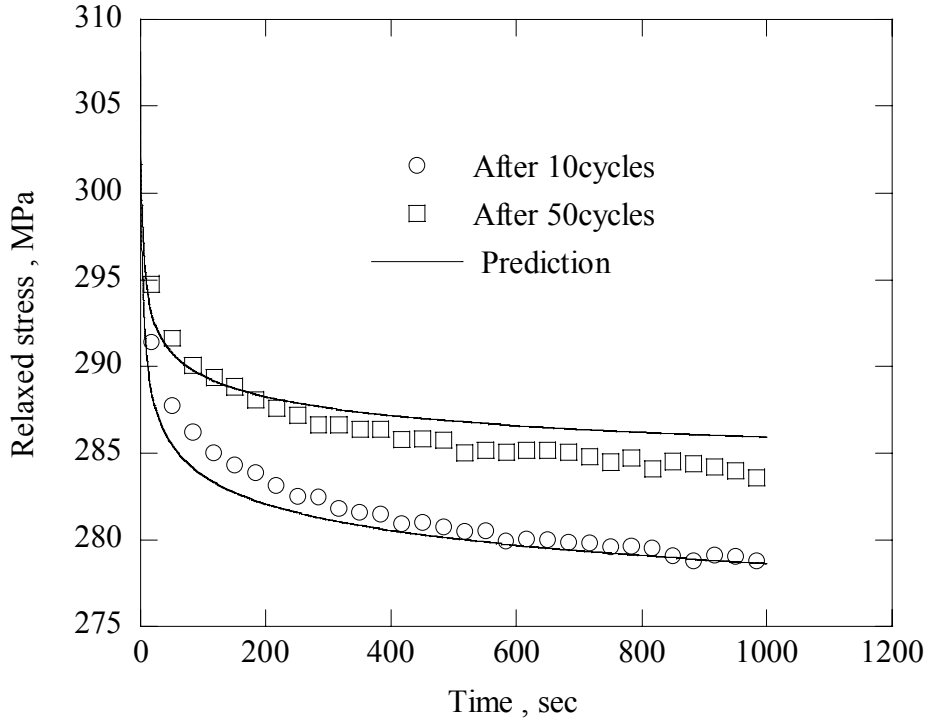

Fig.9 Stress relaxation curves of subsequent stress relaxation tests at a strain of 0.5% after 10 and 50 cycles of cyclic loading with model predictions

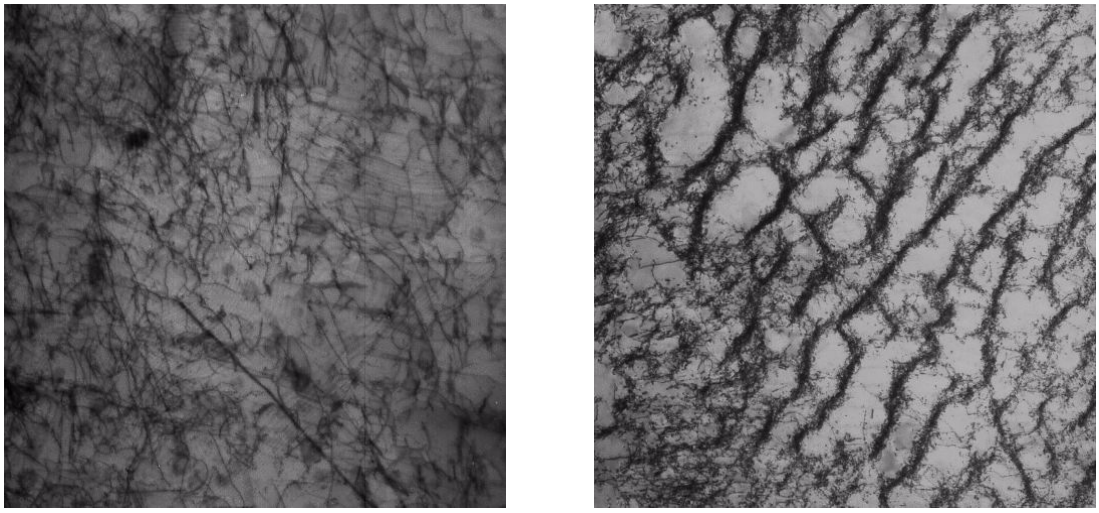

(a) After 10 cycles (b) After 50 cycles

Fig.10 Micrographs of dislocation structures after cyclic loading in Type316L stainless steel

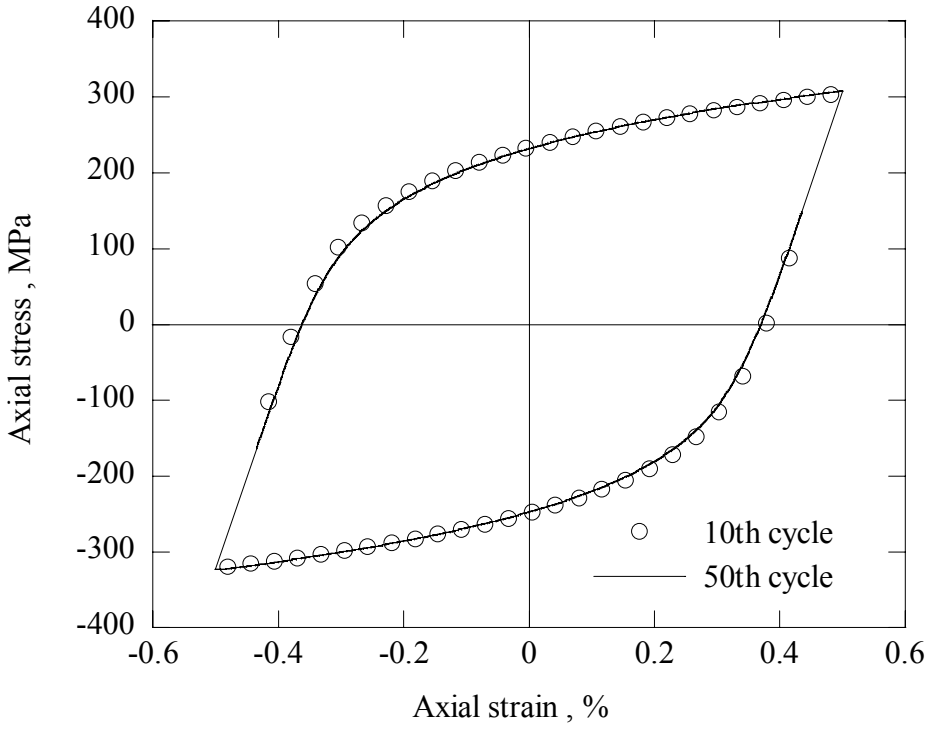

Fig.11 Predicted stress-strain curves of the 10^{th} and 50^{th} cycle of cyclic loading

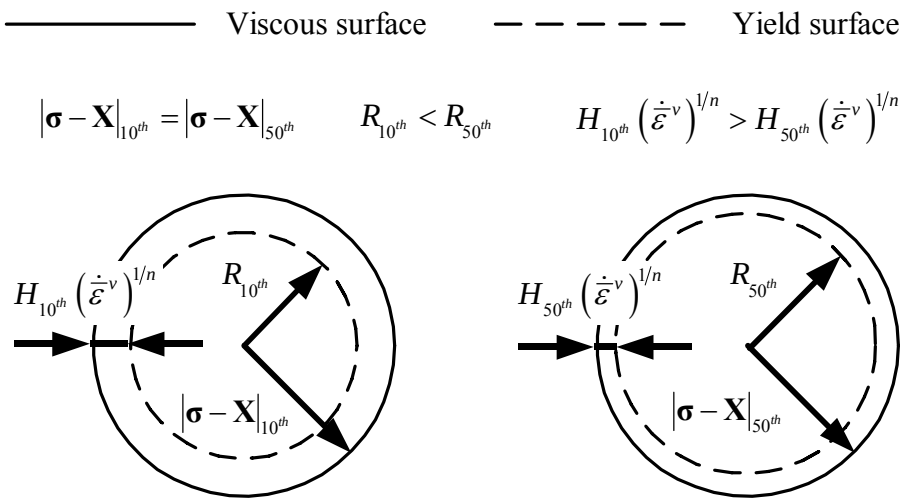

(a) After 10 cycles (b) After 50 cycles

Fig.12 Schematic diagram of change in yield surface and viscous surface

Table 1　Material parameters of Type 316L stainless steel

K [MPa]	D_0 [MPa]	a_h	α_h	m_0	b	R_0 [MPa]	c	λ	
0.05	110	0.1	0.37	6	0.1	130	0.01	0.1	
E [GPa]	D_1 [MPa]	a_s	α_s	m_1	β	H_{sat} [MPa]	n	η	h_s
200	175	0.55	0.02	4.5	0.1	110	7	0.6	0.2